Hindawi
International Journal of Energy Research
Volume 2023, Article ID 9215680, 17 pages
https://doi.org/10.1155/2023/9215680

Research Article

All-Vacuum-Deposited Bifacial $Cu_2ZnSnSe_4$ Photovoltaic Cells with Sputtered Cd-Free Buffer Layer

Fang-I Lai,[1] **Jui-Fu Yang**,[1] **Wei-Chun Chen**,[2] **Yu-Chao Hsu**,[3,4] **and Shou-Yi Kuo**[3,5]

[1]*Department of Electrical Engineering Program C, Yuan Ze University, 135 Yuan-Tung Road, Chung-Li, 32003, Taiwan*
[2]*Taiwan Instrument Research Institute, National Applied Research Laboratories, HsinChu 30076, Taiwan*
[3]*Department of Urology, Chang Gung Memorial Hospital, Linkou, No. 5, Fuxing Street, Kwei-Shan, Taoyuan 333, Taiwan*
[4]*School of Medicine, Chang Gung University, 259 Wen-Hwa 1st Road, Kwei-Shan, Taoyuan 333, Taiwan*
[5]*Department of Electronic Engineering, Chang Gung University, 259 Wen-Hwa 1st Road, Kwei-Shan, Taoyuan 333, Taiwan*

Correspondence should be addressed to Shou-Yi Kuo; sykuo@mail.cgu.edu.tw

Received 14 September 2022; Revised 23 November 2022; Accepted 12 December 2022; Published 3 February 2023

Academic Editor: Pawan Kumar Kulriya

By depositing metal precursors on fluorine-doped tin oxide substrates using evaporation and postselenisation and modifying the number of stacked metallic precursor layers, this study systematically analysed the effect of cation changes on the absorber layer and the solar cell properties of $Cu_2ZnSnSe_4$ (CZTSe). Furthermore, in this study, an all-vacuum method was adopted to prepare a cadmium-free bifacial CZTSe solar cell and conducted damp heat tests on the device. The findings indicate that the increase in the number of stacked metallic precursor layers suppresses secondary phase generation, thereby enhancing the film performance and bifacial solar cell characteristics. The cadmium-free bifacial CZTSe solar cell prepared in this study exhibited the efficiency of 4.13% under bifacial incident light. Moreover, the degradation of the device was effectively mitigated in the damp heat tests compared with previously reported devices with metal substrates. These findings can provide new directions for research and lead to novel applications for CZTSe solar cells in the future.

1. Introduction

Kesterite CZTS(Se) has an absorption coefficient that is greater than $10^4\,\mathrm{cm}^{-1}$ in the visible spectrum, and its energy bandgap can be modulated by cation-alloying or anion-alloying, making it highly suitable for use in high-efficiency solar cell and tandem solar-cell applications [1, 2]. As opposed to organic perovskite solar cells and inorganic $Cu(In,Ga)Se_2$ (CIGS) solar cells, CZTS(Se) is composed of low-cost elements and has the potential for mass production. Many studies have indicated that the composition ratio of cations in CZTS(Se) thin film has a significant influence on the photovoltaic conversion efficiency of CZTS(Se) thin-film solar cells. It is therefore crucial to adjust and optimise the ratio of cations in CZTS(Se) thin-film solar cells to improve their photovoltaic conversion efficiency [3–5].

At present, most CZTS(Se) solar cells adopt an SLG/Mo/CZTS(Se)/CdS/i-ZnO/TCL structure [6–10], which are not only unfriendly to the environment but also have problems with component integration and application. Mo is typically used as the electrode because it forms an interface layer of $MoS(Se)_2$ between the absorber layer during high-temperature sulphurisation (selenisation). An $MoS(Se)_2$ layer of appropriate thickness has good adhesion properties and exhibits ohmic contact with the absorber layer [11]. However, when the $MoS(Se)_2$ layer is too thick, it creates a nonohmic contact between the Mo back electrode and the absorber layer, thus hindering the carrier injection of the absorber layer to the Mo back electrode [12]. Moreover, when a metal substrate is used as the back electrode, only the front incident light can be received, thus restricting the application of photovoltaic integration in architectural design. At present, the most common commercial transparent conductive substrates are SnO_2:F (FTO) and In_2O_3:SnO_2 (ITO) substrates. However, indium tin oxide (ITO) materials are produced in small quantities and are relatively expensive due the use of a precious metal, indium (In), while the current panel factories still use ITO as the main transparent contact layer (TCL). The In atoms in the ITO substrate can diffuse into the adsorber layer at high temperatures, causing the conductivity of the back electrode to deteriorate, and rendering the ITO substrate unsuitable for application in solar cells [13, 14]. The highest efficiency attained for CZTS(Se) is 13.2% in the nonvacuum process currently [15], followed by 12.62% in the vacuum process [16]. The currently lower efficiency of CZTS(Se) compared to CIGS can be primarily attributed to the lower open-circuit voltage (V_{OC}) and the lower fill factor [17]. Most studies attribute the lower V_{OC} primarily to the secondary phases in the absorber layers, smaller grain size, and CuZn antisite defects, of which the secondary phases are the most significant factor in relation to CZTS(Se). The common secondary phases in the CZTS(Se) absorber layers are Cu–Se, Zn–Se, Sn–Se, and Cu–Sn–Se compounds. In addition, the presence of secondary phases on the surface of the absorber layer film also affects the coverage of the junction of the deposition buffer layer. The appearance of $Cu_xS(Se)$ and $SnS(Se)_x$ secondary phase on the surface of the prepared absorber layer can greatly reduce device efficiency, as these secondary phase contain a trap level, forming nonradiative recombination centres [18]. This not only affects the energy bandgap of the absorber layer but can also decrease the number of conducting paths for carriers, increase the series resistance, and decrease the open-circuit voltage and the fill factor of solar cells [19]. To improve the efficiency of CZTS(Se) solar cells, scholars have suggested suppressing secondary phases by changing the cation ratio in the CZTS(Se) film during the deposition, as well as removing the secondary phase from the surface of the films using various etching solutions. However, although these chemical solutions can remove the secondary phases, they also affect the chemical homogeneity of the composition of CZTS(Se) films. Furthermore, after etching, bandgaps would form on the surfaces and bottoms of the films, undermining the quality of CZTS(Se) films [20]. Moreover, not all of these chemical solutions are environmentally friendly. In addition to the above methods, Li et al. used temperature regulation to control the chemical environment of atoms, further changing the atomic oxidation state and formation of shallow/deep defects, thereby effectively suppressing the intrinsic defects and activating desirable shallow acceptor Cu vacancies in the absorber layer. This can substantially improve the film quality [21]. Lastly, the buffer layer (cadmium sulphide, CdS) film is commonly deposited using chemical bath deposition (CBD) method, which cannot be integrated into a continuous manufacturing process. In addition, the waste liquid remaining after CBD and the Cd found in CdS thin films are not environment-friendly. Also, the energy bandgap of CdS thin films is approximately 2.44 eV, which causes some light in the green to ultraviolet range to be absorbed or lost, resulting in a decrease in the overall device efficiency. As a result, CZTS(Se) solar cells without a Cd buffer layer have garnered much attention [22, 23].

In summary, the research on cadmium-free bifacial CZTSe solar cells is important for sustainable development. After revisiting the recent developments in bifacial CZTS(Se) solar cells, we found that CZTSe elements on FTO substrates produced using the nonvacuum spin-coating from precursor solution paste exhibit a maximum efficiency of 2.2% [24]. Recently, Ge et al. prepared bifacial CZTS solar cells on ITO substrates by adopting a codeposition method; the efficiency of such solar cells reached 3.4% under bifacial incident light [25]. Mali et al. produced CZTS solar cells on FTO substrates using successive ionic layer adsorption and reaction, with efficiency reaching 1.85% under front incident light [26]. Regarding the preparation of bifacial CZTS(Se) solar cells via the vacuum process, Moises et al. produced CZTS(Se) solar cells on FTO substrates by adopting the sputtering and postselenisation (selenium, sulfur) method; the efficiency of these cells reached 3.1% [27] under bifacial incident light. Kim et al. fabricated CZTSe solar cells on FTO and ITO substrates using sputtering and postselenisation; the efficiencies of the prepared solar cells reached 6.05% for FTO substrate and 4.31% for ITO substrate under bifacial incident light, which are the highest reported efficiencies as of now [28]. Thus, the vacuum method is more advantageous for the fabrication of the bifacial kesterite solar cells. Moreover, the vacuum process offers the advantages of mature technology, stability, and high yield compared with the nonvacuum process. In addition, the CIGS were initially made using the vacuum process. In the common vacuum-manufacturing processes, the evaporation and postsulfurization/-selenisation method is highly effective in controlling the cation modulation of CZTS(Se). This is because, as compared to other vacuum methods, evaporation makes it easier to control the cation ratio of the CZTS(Se) precursor film without wasting the raw materials. The evaporation and postsulfurization/-selenisation process often uses pure metal, homogeneous mixtures, or sulphur (selenium)-containing compounds. After depositing the precursor film on the back electrode, high-temperature postsulfurization/-selenisation is carried out to form the CZTS(Se) absorber layer. Compared to homogeneous mixtures, or sulphur/selenium-containing compounds, pure metal precursors have the advantages of lower machinery costs and easier control over the ratio of cations. In the structural design of a pure metal precursor stack, using Sn as the bottom layer can improve the adhesion between the thin film and the back electrode (dewetting effect) [29]; while using Cu as the capping layer can effectively prevent the underlying Zn/Sn bilayer from being volatile during high-temperature postsulfurization/-selenisation, thus inhibiting the formation of secondary phases. In addition, adopting Cu as the bottom layer can generate an unstable interface with the back-electrode metal, Mo [30]. Considering these factors, the common structure of a metal precursor stack is as follows: back electrode/Sn/Zn/Cu [31, 32]. However, according to the diffusion table of the Cu/Zn/Sn matrix [33], although Sn and Zn (which are adjacent to each other) have good interdiffusion coefficients at high temperature, Cu and Zn (which are also adjacent to each other) have poor interdiffusion coefficients at high temperature. This could lead to nonuniform distribution of cations, which, in turn, affects the film quality and device efficiency. Therefore, it is important to explore different methods to mitigate the problem of interdiffusion of cations. To solve the problem on film uniformity of the absorption layer, Yang et al. used a multilayered precursor structure on the Mo foil substrate. This improves film uniformity; simultaneously, it suppresses Sn-related donor defects and the Sn-related secondary phase [34].

In view of the issues above, this study employed the evaporation and postselenisation method to deposit metal precursors on a fluorine-doped tin oxide (FTO) substrate and modified the thickness and the number of metal precursor stacks (while keeping the total thickness of each metal unchanged). The goal was to promote the interdiffusion between the metallic layers and convert the metallic phase into an alloy phase while suppressing the generation of secondary phases such as Cu_xSe and Cu_2SnSe_3 (CTSe) without treatment with solutions. Changes in optical and thin film quality were also investigated. Furthermore, this study adopted the sputtering method to deposit $Zn_{0.75}Sn_{0.25}O$ (ZTO) to replace CdS as a buffer layer. Compared with the current bifacial CZTS(Se) solar cells, in which CdS buffer layer is still deposited using CBD, bifacial CZTSe solar cells produced in this study are more eco-friendly. However, the most significant improvement is that the photovoltaic conversion efficiency of CZTSe solar cells is 3.89% under front incident light and 4.13% under bifocal incident light. Furthermore, damp heat (DH) tests on cadmium-free bifacial CZTSe solar cells were also conducted in this study. The findings show a significant improvement in the decay rate of bifacial CZTSe solar cells fabricated on FTO substrates compared with CIGS and CZTS(Se) solar cells with Mo as the back electrode. However, the efficiency decreased by a significant extent compared with solar cells with FTO substrates (reported in other studies). This result may be attributed to the insufficient optimisation of the ZTO buffer layer, which will be addressed in the future.

2. Experimental

In this study, CZTSe thin-film solar cells were prepared using evaporation and postselenisation, and the manufacturing process is shown in Figure 1. First, the Sn/Zn/Cu metal precursors were sequentially deposited by evaporation on a commercially available FTO glass substrate at room temperature. The metal used for vapor deposition had a purity of 99.999% (purchased from Summit-Tech Resource Corp.); commercial FTO with a sheet resistance of approximately 20 Ω/□ (Ruilong Optoelectronics Co., Ltd.). The stacked precursor layers were numbered as follows: 1-cycle-P was defined as the metal precursor (FTO/Sn/Zn/Cu), while 2-cycle-P divided 1-cycle-P into two groups (FTO/Sn/Zn/Cu/Sn/Zn/Cu), with the total thickness of each metal remaining constant. Similarly, the 1-cycle-P was divided into three groups (FTO/Sn/Zn/Cu/Sn/Zn/Cu/Sn/Zn/Cu) and four groups (FTO/Sn/Zn/Cu/Sn/Zn/Cu). The 3-cycle-P and 4-cycle-P specimens were defined accordingly. Subsequently, the metal precursor specimens were placed with 700 mg of solid Se (99.999% purity; Summit-Tech Resource Corp.) in a quartz box, which was then placed in a tube furnace. Pure argon (Ar, 5 N) gas was introduced in the furnace, and a three-stage selenisation process was carried out. All the specimens were then removed from the furnace and allowed to cool down naturally. The precursor specimens after the three-stage postselenisation were designated as 1-cycle (for 1 cycle-P), 2-cycle (for 2-cycle-P), 3-cycle (for 3-cycle-P), and 4-cycle (for 4-cycle-P) specimens. X-ray diffraction (XRD), field emission scanning electron microscopy (FE-SEM; JXA-8530F Pus, JEOL), energy dispersive spectroscopy (EDS), UV-Vis-NIR spectroscopy (V670, JASCO), Raman microspectroscopy, atomic force microscopy (AFM; Innova SPM, Bruker), and transmission electron microscopy (TEM; JEM-F200, JEOL) were performed to analyse the structure, morphology, optical properties, electrical properties, the microstructure of the thin film, and the changes in the thin-film quality. XRD analysis was performed using a SIEMENS D500 X-ray instrument with Cu Kα (1.5418 Å) radiation, scanned at 0.005 in an angular 2θ range of 10–80° at an integration time of 1 s. Raman microspectroscopy measurements were conducted using an Ar laser (514 nm) matching a triple monochromator (Horiba Triax, Jobin Yvon) combined with a TE-cooled CCD detector, at room temperature.

After preparing the absorber layer, a ZTO (99.999% purity) buffer layer with a thickness of approximately 50 nm was deposited by sputtering at a substrate temperature of 90°C, working pressure of 1.5 mTorr, and RF power of 25 W in Ar gas. Subsequently, a layer each of i-ZnO (99.95% purity), AZOY (99.95% purity), Ni (99.99% purity), and Al (99.999% purity) with an approximate thickness of 50 nm, 300 nm, 50 nm, and 1 μm, respectively, were deposited. Ni and Al layers were deposited by sputtering, and the resultant specimen was used as the upper electrode. All target materials had a dimension of three inches and were purchased from Summit-Tech Resource Corp. After completing the bifacial CZTSe solar cell, the current density–voltage (J–V) curve was measured to determine the photovoltaic characteristics of the device. The ambient temperature during the measurement was controlled at 25 ± 1°C. The J–V measurements performed herein can be divided into single measurements with front, rear, and bifacial incident light. The measurement with front incident light was performed in an environment with a solar simulator (Newport 94022A) that generated an AM 1.5 global standard spectrum with a light intensity of 1000 W m^{-2} (i.e., 1 sun), whereas the measurement with bifacial incident light was performed in an environment where a light intensity of 1 sun was reflected by a 45° mirror onto the rear of the device. Thus, the light intensity values at the front, rear, and both sides were 1 sun, 0.3 sun, and 1.3 sun, respectively. In addition, the EQE spectra of the specimens were obtained using a 300 W xenon lamp (Newport 66984) light source and a monochromator (Newport 74112). The spot projected on the specimen was approximately 1 mm × 3 mm in size. DH measurements were conducted using Espec LHU-113 at a temperature of 85°C and relative humidity (RH) of 85%.

3. Result and Discussion

Figures 2(a)–2(h) show the SEM images of the top- and the cross-sectional views of the CZTSe films of the 1-cycle, 2-cycle, 3-cycle, and 4-cycle specimens, respectively. The atomic percentage in the cross sections was measured with EDS, and the results are listed in Table 1. It can be seen from Figures 2(a)–2(d) that large grains of approximately 5 μm (indicated by red outlines) are formed on the surfaces of the 1-, 2-, and 3-cycle specimens. According to the literature, we expected these layers to be Cu_xSe compounds. In CZTSe thin films, the formation of the Cu_xSe secondary phase creates a leakage path, which can affect the device interface [35]. In addition, as the number of precursor stacked layers

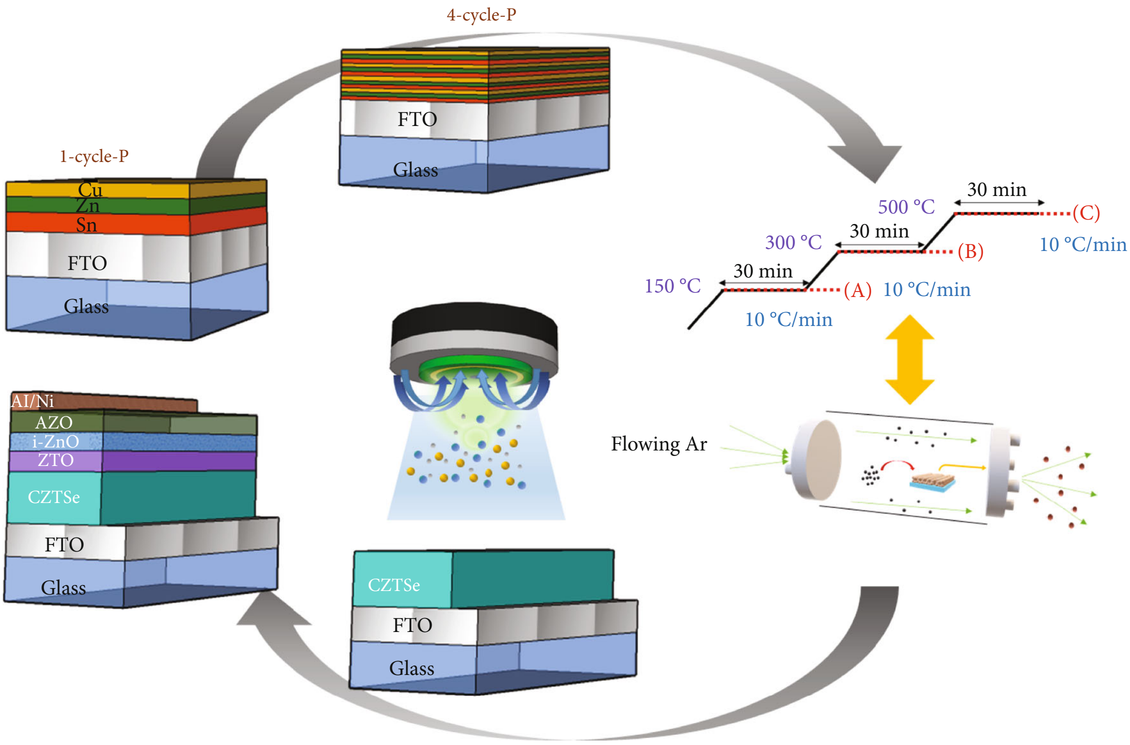

Figure 1: Schematic diagram of experiment. In this experiment, the most basic 1-cycle-P precursor was gradually modified into a 4-cycle-P precursor. Subsequently, after completing the selenisation reaction (using three-stage heating), the film of the CZTSe absorption layer was produced. Subsequently, the buffer layer, window layer, and upper electrode were deposited by sputtering. In the inset, (a), (b), and (c) labelled on the heating curve are the measurements obtained after staged heating and taking the test piece out in order to further understand the difference between the reaction mechanism of 1-cycle-P and that of 4-cycle-P.

increased, the secondary phase gradually decreased in size. The 4-cycle specimen no longer showed any obviously large grains on the surface. It can be seen from the cross-sectional views that all CZTSe thin films had a thickness of approximately 1.5 μm, with good adhesion to the FTO substrate. We also measured the profile atomic percentages of 1-, 2-, 3-, and 4-cycle-P profiles of specimens by EDS. All precursor specimens were Cu-depleted ($Cu/(Zn + Sn) < 1$) and Zn-rich ($Zn/Sn > 1$), and the atomic percentages were similar for different numbers of stacked precursor layers. The results are also listed in Table 1.

Figures 2(i)–2(l) show AFM measurements of the 1-cycle, 2-cycle, 3-cycle, and 4-cycle specimens, respectively. It can be seen that while the surface roughness values for the 1-cycle, 2-cycle, and 3-cycle specimens were generally the same, the 4-cycle specimen had a relatively low surface roughness, which could be due to the relatively good interdiffusion of metals in the precursor of the 4-cycle specimen. A thin film containing an absorber layer with a rough surface can lead to poor interface quality between the absorber and buffer layers, thus further reducing the conversion efficiency. Table 1 lists the atomic percentages of the 1-cycle, 2-cycle, 3-cycle, and 4-cycle specimens. It can be seen from the table that as the number of precursor stacked layers increased, the maximum relative changes of Se, Cu, Zn, and Sn atoms were 2.11%, 6.96%, 15.25%, and 37.7%, respectively, with Sn atoms showing the highest relative change. We speculated that the relative changes in the atomic percentages were due to the increase in the number of metal precursor stacks. In other words, there was a relative increase in Cu-Sn interfaces, and since Cu is highly diffusible, it might form Cu_6Sn_5 alloy with Sn (see below for more details). This suppressed the loss of Sn atoms during high-temperature selenisation, thus leading to a higher Sn atomic percentage.

Figure 3(a) shows the XRD measurements of the 1-cycle, 2-cycle, 3-cycle, and 4-cycle specimens (raw data subjected to log processing). All the specimens showed the (112), (204), (312), and (316) diffraction peaks of CZTSe, as well as the diffraction peak of the FTO substrate, at 33.8°, 51.6°, and 65.6°. The (311), (312), (006), and (318) diffraction peaks of the Cu_xSe secondary phase could be observed in the 1-cycle, 2-cycle, and 3-cycle specimens, with the intensity decreasing as the number of precursor stacked layers increased. The 4-cycle specimen showed no obvious diffraction peak for Cu_xSe, indicating that it had better thin-film quality. XRD is a macroscopic measurement, and CZTSe has diffractions peaks that are located close to those of many secondary phases, which makes them difficult to distinguish. Therefore, Raman spectroscopy was performed to fully understand the formation of the relevant compounds. Figure 3(b) shows the spectra of the 1-cycle, 2-cycle, 3-cycle, and 4-cycle specimens under the A1 Raman mode (after the data were normalised). In general, clear signals can be observed at 190–192 cm^{-1} and 169–171 cm^{-1}, both corresponding to CZTSe [36, 37]. As the number of precursor

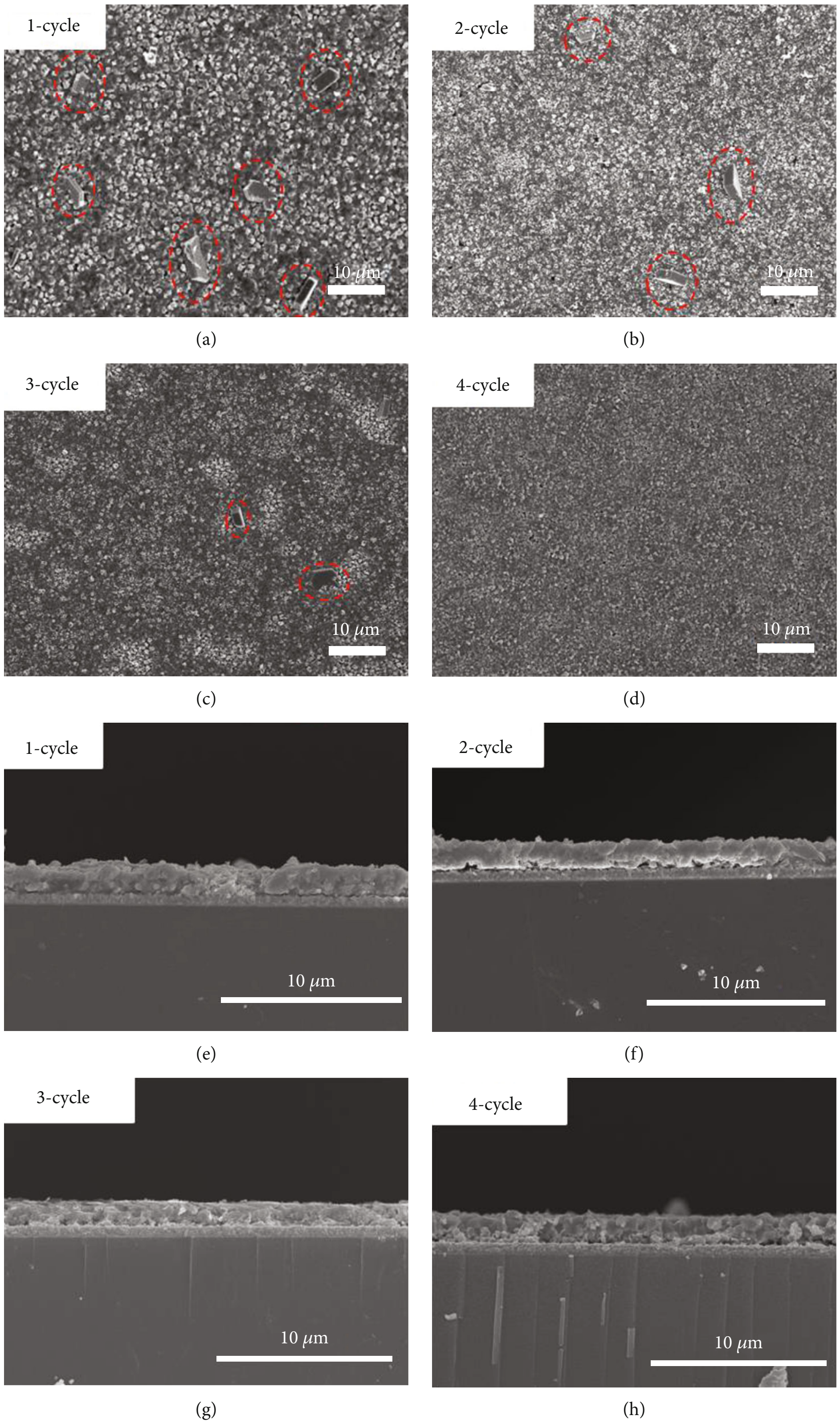

(a) (b) (c) (d) (e) (f) (g) (h)

Figure 2: Continued.

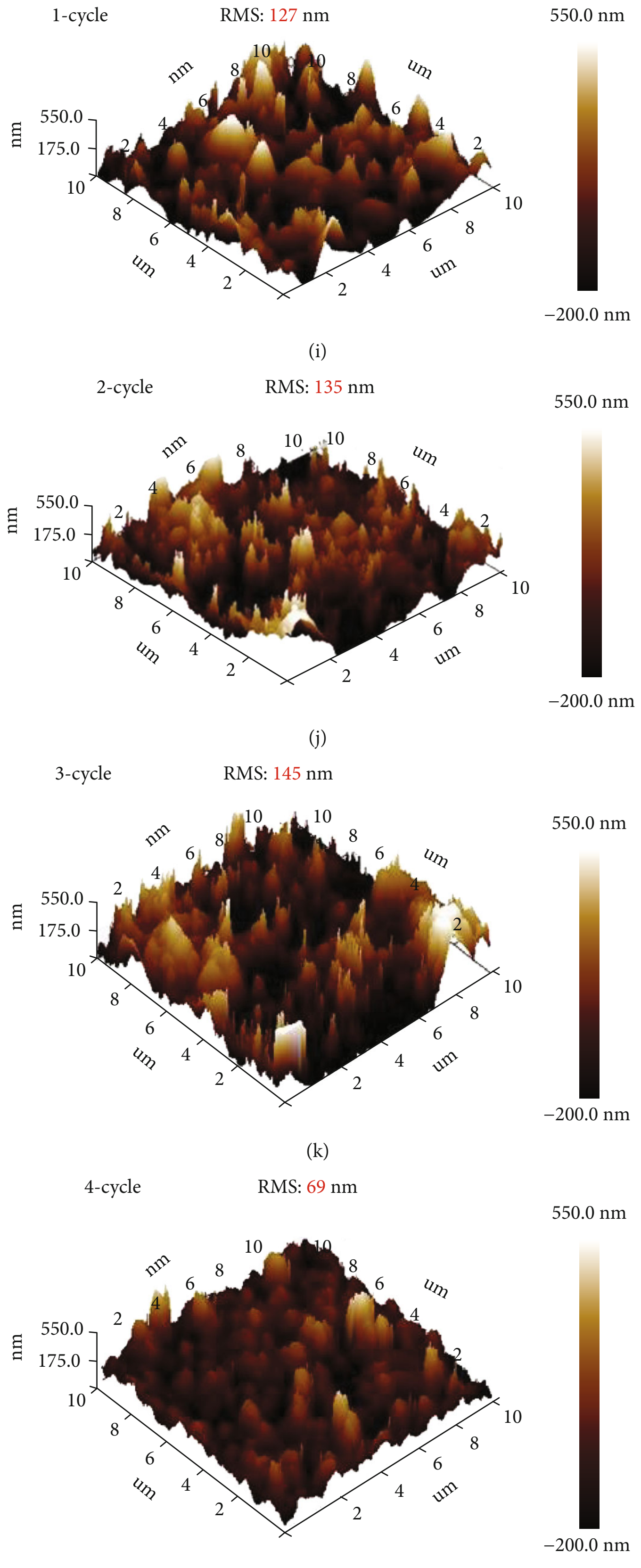

(i)

(j)

(k)

(l)

Figure 2: (a–d) SEM top views of the 1-cycle, 2-cycle, 3-cycle, and 4-cycle specimens, respectively; (e–h) cross-sectional views of the 1-cycle, 2-cycle, 3-cycle, and 4-cycle specimens, respectively; (i–l) AFM measurements of the 1-cycle, 2-cycle, 3-cycle, and 4-cycle specimens, respectively.

Table 1: Number of stacked layers of different precursors and atomic percentages of CZTSe absorber layers measured by EDS.

	Cu (%)	Zn (%)	Sn (%)	Se (%)	Cu/(Zn + Sn)	Zn/ Sn
1-Cycle	26.14	15.74	8.41	49.71	1.08	1.87
2-Cycle	25.95	15.53	9.03	49.49	1.06	1.72
3-Cycle	25.68	14.49	10.45	49.38	1.03	1.39
4-Cycle	24.32	13.34	11.58	50.76	0.98	1.15
1-Cycle-P	47.15	28.83	24.02		0.89	1.2
2-Cycle-P	47.03	28.87	24.1		0.89	1.2
3-Cycle-P	47.02	28.85	24.13		0.89	1.2
4-Cycle-P	46.99	28.86	24.15		0.89	1.2

stacked layers increased, the main signal peak of CZTSe gradually moved towards the low-frequency range. This phenomenon may be related to the following equation [38]:

$$\upsilon(A_1) = \sqrt{\frac{2\alpha_{\mathrm{Cu-VI}} + \alpha_{\mathrm{Zn-VI}} + \alpha_{\mathrm{Sn-VI}}}{M_{\mathrm{VI}}}}, \qquad (1)$$

where α is the bond stretching force constant and X–VI follows (X = Cu, Zn, Sn, and VI = Se). As shown in to Table 1, the Se anions showed minimal changes, whereas the Cu, Zn, and Sn cations all showed changes, which may have caused the shift.

To further confirm whether the large grains on the thin-film surface were indeed the $\mathrm{Cu_xSe}$ phase seen in the SEM image, as well as to understand the changes in the distribution of the $\mathrm{Cu_xSe}$ phase on the absorber layer surface, Raman mapping was used to study the surface of each specimen. Figures 4(a)–4(d) show the Raman maps the 1-cycle, 2-cycle, 3-cycle, and 4-cycle specimens. Under the A1 mode, the large grains were defined as the $\mathrm{Cu_xSe}$ secondary phase in the frequency range of 240–289 $\mathrm{cm^{-1}}$, thereby showing the composition distribution of the $\mathrm{Cu_xSe}$ secondary phase in the planar space. The $\mathrm{Cu_xSe}$ clusters on the surface of the 1-cycle specimen were 2–8 μm in size, which were much larger than the CZTSe grains. However, as the precursor stack layers increased in number, the $\mathrm{Cu_xSe}$ clusters on the surfaces of the 2-cycle and 3-cycle specimens decreased in size. For the 4-cycle specimen, only a small amount of $\mathrm{Cu_xSe}$ clusters remained. The Raman mapping analysis demonstrated that as the number of precursor stacked layers of the specimen increased, the $\mathrm{Cu_xSe}$ clusters on the specimen surface gradually decreased in number, which was consistent with the previous XRD and SEM measurement results.

Since Raman spectroscopy only measures signals to a depth of approximately 220 nm below the specimen surface, UV–vis–NIR spectra were used to further understand the internal structure of the CZTSe thin film and determine its quality. Figures 5(a) and 5(b) show the transmittance/reflectance and absorptance values, respectively, of the 1-cycle, 2-cycle, 3-cycle, and 4-cycle specimens deposited on the FTO substrate, as measured by UV–vis–NIR spectroscopy. Figure 5(a) shows no significant changes in the reflectance characteristics of the four specimens before 1200 nm. It is worth noting that the reflectance of the 4-cycle specimen increased significantly after 1200 nm, whereas that of the 1-cycle, 2-cycle, and 3-cycle specimens showed no significant changes. The variation in reflectance was primarily attributed to the effects of material properties and surface topography, whereas the change in the reflectance of the films was primarily attributed to the refractive index of the materials and the roughness of the surface. Hirate et al. and Yadav et al. revealed that below 1200 nm, the trends of the change in the refractive index of CZTSe, $\mathrm{Cu_xSe}$, and CTSe are virtually the same [39, 40]. Thus, little change occurred in the reflectance characteristics of the four samples. However, from 1-cycle to 3-cycle, the reflectance gradually decreased as the number of stacked precursor layers increased, probably because of the decrease in the amount of CTSe and $\mathrm{Cu_xSe}$ in the films. The simplified thin-film optical model suggested that the higher the refractive index of the material, the higher the reflectance. The refractive indexes of CTSe and $\mathrm{Cu_xSe}$ were higher than that of CZTSe. As the amount of CTSe and $\mathrm{Cu_xSe}$ decreased, the reflectance decreased. Secondly, we investigated the effects of surface roughness on reflectance. As shown in the AFM measurements in Figures 2(i)–2(l), little change occurred in the surface roughness from the 1-cycle specimen to the 3-cycle specimen. Hence, the effects of surface roughness were not considered. However, the surface roughness of the 4-cycle specimen was greatly reduced; thus the absorber layer had a mirror-like surface and exhibited the highest reflectance. In terms of transmittance, all the four specimens showed no obvious changes before 800 nm, but changes began to occur after 800 nm, and were especially significant in the 4-cycle specimen. It was speculated that the above changes in the transmittance and reflectance values were due to material absorptance. The absorptance values obtained based on absorptivity (penetration rate)/reflectance calculations are shown in Figure 5(b) and can be divided into zone (I), zone (II), and zone (III). In zone (I), all the specimens had high absorptance, but the absorptance values of the 1-cycle, 2-cycle, and 3-cycle specimens were higher than that of the 4-cycle specimen. In zone (II), the absorptance of the 4-cycle specimen decreased sharply, showing an obvious absorption boundary for CZTSe at 1.16 eV, whereas all the other specimens still showed high absorptance because the energy bandgap of the CTSe secondary phase was between 0.84 eV and 2.1 eV [41]. Therefore, it was speculated that the changes caused were due to the absorption properties of the CTSe material. In zone (III), the absorptance of the 4-cycle specimen increased, presumably owing to the characteristics of the FTO thin film. In comparison, the 1-cycle, 2-cycle, and 3-cycle specimens still had relatively high absorptance values. The presence of CTSe in the CZTSe thin film can lead to electricity leakage [42]. This phenomenon may have occurred because the metal precursors of the 1-cycle, 2-cycle, and 3-cycle specimens were not sufficiently thin, resulting in the incomplete and nonuniform diffusion

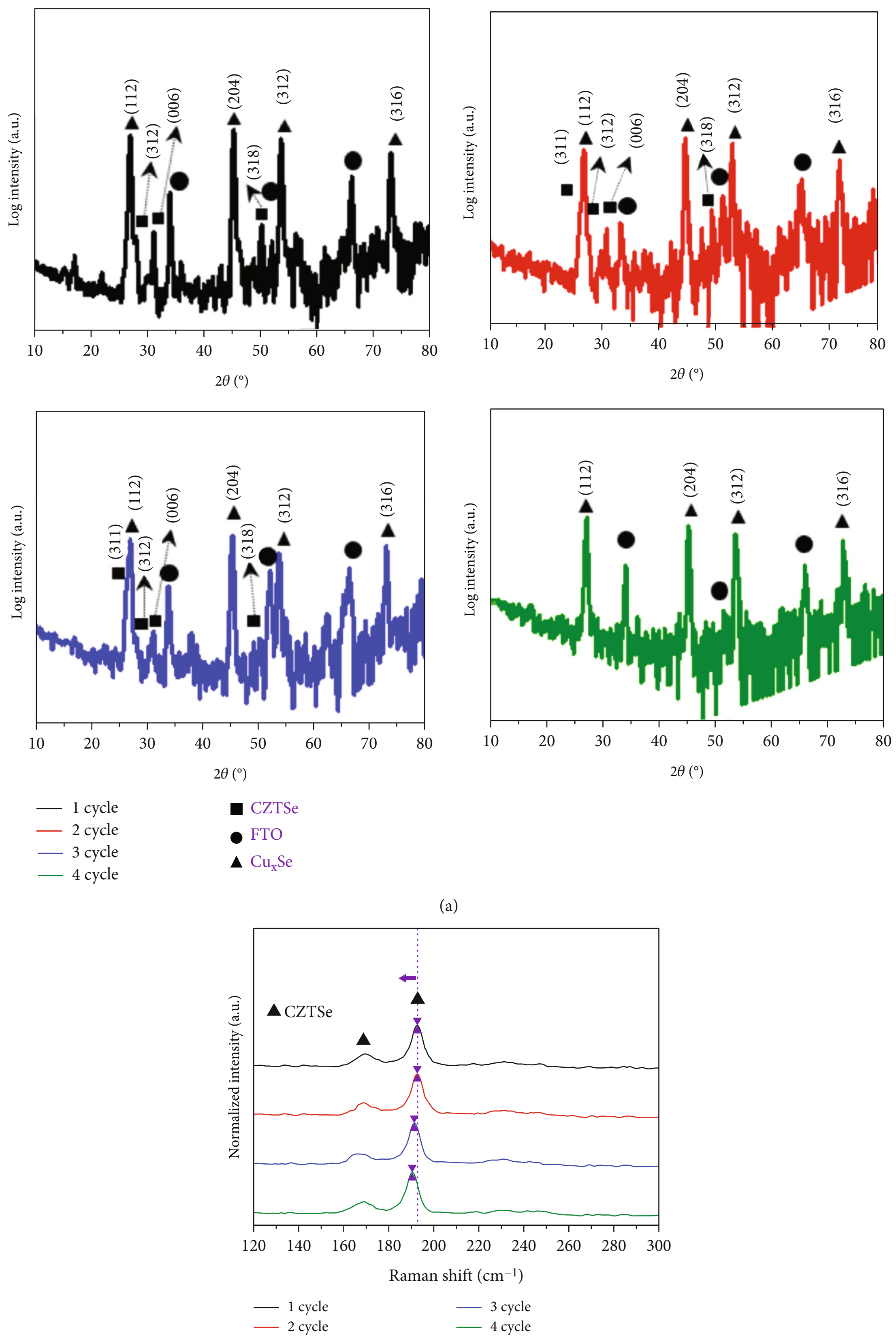

(a)

(b)

Figure 3: (a) XRD measurements, and (b) Raman spectrum measurements of the 1- to 4-cycle specimens.

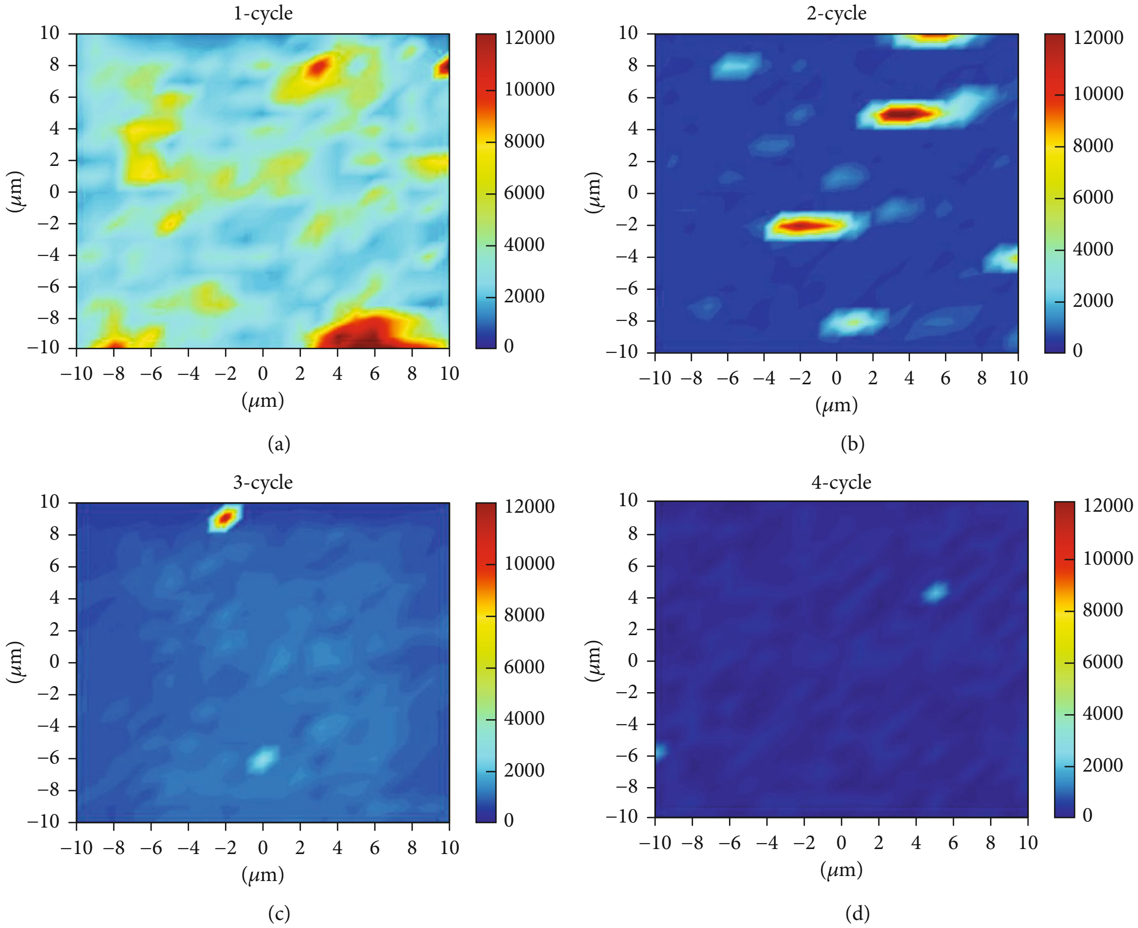

(a)

(b)

(c)

(d)

Figure 4: (a–d) Raman maps of the 1-cycle, 2-cycle, 3-cycle, and 4-cycle specimens, respectively. The scale bars in the figure are the Cu_xSe signal strength.

between the metal precursors. The absorption coefficient of the bandgap energy of the CZTSe thin film can be obtained from the intercept on the axis of the photon energy (hv) when linearly extrapolating the $(ahv)^2$ in the $(ahv)^2$–hv relationship curve [43]:

$$(\alpha h\upsilon)^2 = A\left(\mathrm{hv} - E_g\right), \tag{2}$$

where α is the absorption coefficient, h is Plank's constant, v is the photon frequency, and A is a constant. The energy bandgap calculated from the transmittance/reflectance spectra is shown in Figure 5(c), while Figure 5(d) shows the relationship of the number of precursor stacked layers with energy bandgap and Cu/(Zn + Sn) ratio. It can be seen that as the precursor stacked layers increased in number, the Cu/(Zn + Sn) ratio gradually decreased, and the energy bandgap gradually increased. This may have been due to the hybridisation orbitals formed by the d-orbitals of Cu and the p-orbitals of Se, which resulted in changes consistent with those described in the literature [44].

To confirm that CTSe was present in the 1-cycle specimen, as well as to further understand the quality and the microstructure of the thin film, TEM studies were performed on the 1-cycle and 4-cycle specimens. Figures 6(a) and 6(b) show cross-sectional TEM (XTEM) images of the 4-cycle and 1-cycle specimens, respectively. It can be seen from the two images that the CZTSe film was approximately 1.5 μm in both the cases, and the 1-cycle specimen had a surface that was rougher than the 4-cycle specimen, which was consistent with the AFM results. In addition, the inset in Figure 6(a) shows the HR-XTEM image of the selected area where the electron beam was incident on the crystal in the [100] direction, along with the pattern calculated using a fast Fourier transform (FFT). It can be observed that this CZTSe thin film exhibited a tetragonal structure, which was close to a single-crystal phase. HR-XTEM and/or FFT calculations show the lattice constants to be approximately 0.565 nm for the *a*-axis and approximately 1.156 nm for the *c*-axis, which is consistent with the previously reported results [45]. Figure 6(b) shows regions with different compositions, such as A1 and A2, and these regions were studied separately using HR-XTEM, as shown in Figures 6(c) and 6(d), respectively. Figure 6(c) shows the HR-XTEM measurement for region A1, where the inset shows the pattern of the selected area electron diffraction (SAED), the electron beam being in the [013] direction. This observation confirmed that the 1-cycle specimen contained CTSe with a single-phase cubic

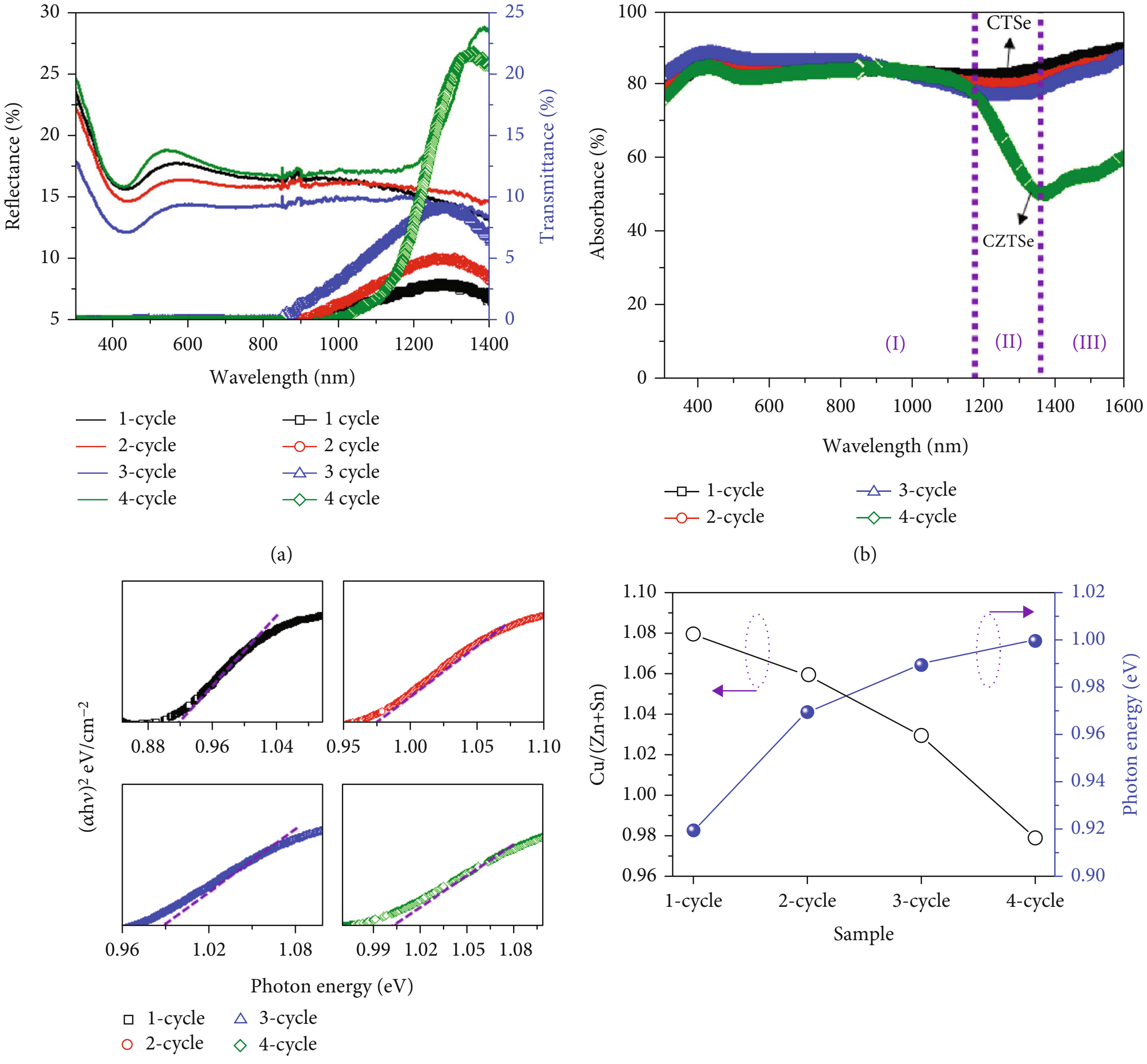

(a)

(b)

(c)

(d)

FIGURE 5: Changes in (a) reflectance and transmittance, (b) absorptance, (c) $(\alpha h\nu)^2$ vs. hν in CZTSe thin film, and (d) optical bandgap of CZTSe thin film with different numbers of metal precursor layers.

structure (where the lattice constant of the *a*-axis was approximately 0.565 nm). Figure 6(d) shows the HR-XTEM measurement for region A2, where the inset shows the pattern calculated using FFT, for which the electron beam was in the [102] direction. It can be seen from the figure that the 1-cycle specimen also contained CZTSe with a tetragonal structure (where the lattice constant was approximately 0.565 nm for the *a*-axis and approximately 1.156 nm for the *c*-axis). This implies that within the 1-cycle specimen, the CTSe secondary phase formed as a result of uneven diffusion between the metal precursors, thus affecting the thin-film quality, which was consistent with the results shown in Figure 5(b).

The aforementioned findings may be summarised as follows: to elucidate the differences in the growth mechanisms of CZTSe films with different numbers of stacked metal precursor layers, we performed selenisation of 1-cycle-P and 4-cycle-P at different temperatures (all experimental parameters were the same as the experimental procedure, with Se solid used), as shown in the heating conditions in Figures 1(a)–1(c). After the reactions at 150°C (a), 350°C (b), and 500°C (c), the specimens were cooled naturally and then removed for XRD (after log treatment) and Raman spectroscopy measurements, as presented in Figure 7(a). The XRD measurements revealed that the precursors of the 1-cycle and 4-cycle specimens both showed the diffraction signals of the Cu_5Zn_8 (PDF 25-1288) alloy, as well as the single elements Cu, Sn, and Zn. Interestingly, the precursor of the 4-cycle specimen contained the Cu_6Sn_5 (PDF 45-1488) bronze alloy (Cu-Sn), and Cu_5Zn_8 exhibited a relatively significant peak. Because the diffusion coefficient of Sn to Zn was extremely small at room temperature, the signal for the Cu-Sn alloy was not detected in the 1-cycle specimen. In contrast, changes in the stacking conditions of the 4-cycle specimen might lead to the formation of the Cn-Sn interface. In the mechanism underlying the formation of CZTSe by metal alloys, bronzes and brasses decompose to form the corresponding

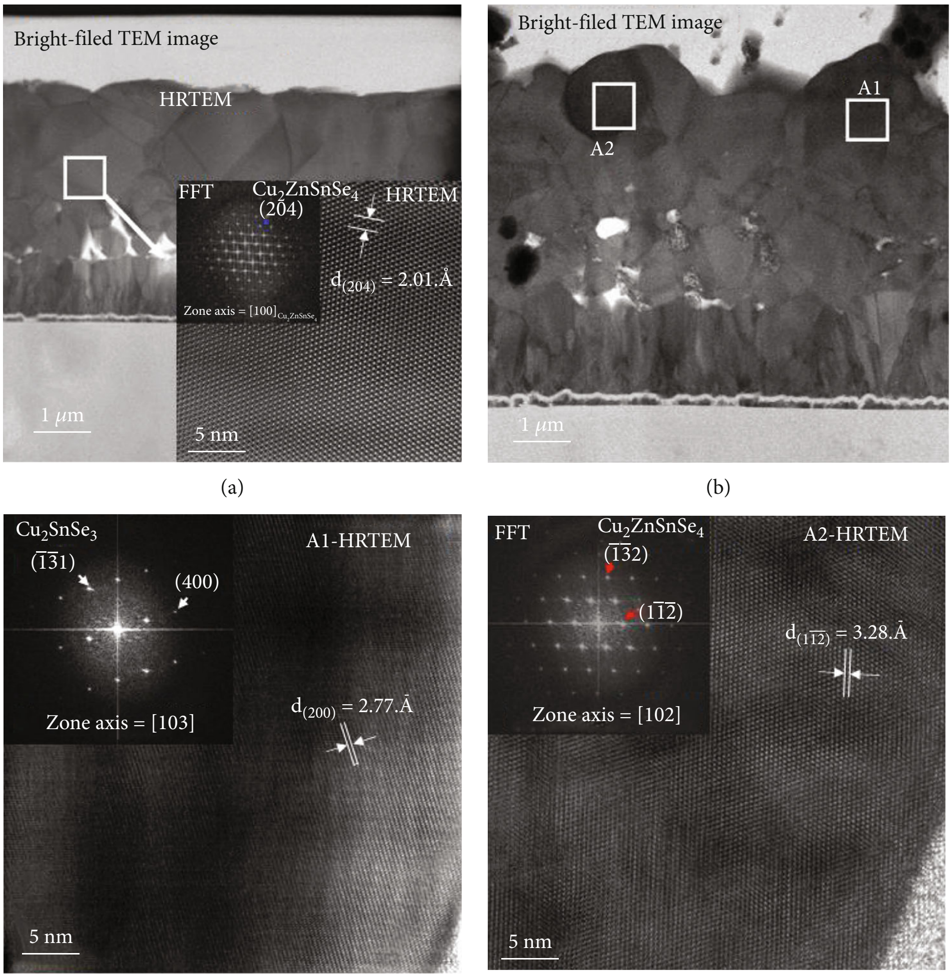

(a) (b)

(c) (d)

Figure 6: TEM images of the (a) 4-cycle specimen and (b) 1-cycle specimen; and HRTEM images of (c) region A1 in the 1-cycle specimen and (d) region A2 in the 1-cycle specimen.

compounds at the given temperature. This is very important for CZTSe, which requires a precise crystal structure [46]. In addition, the formation of the Cu_6Sn_5 alloy could also contribute to the growth of CZTSe grains [47]. When the specimens underwent selenisation at 150°C, the 4-cycle specimen showed even more significant signals for Cu_6Sn_5 and Cu_5Zn_8, and the 1-cycle specimen also showed a stronger signal for Cu_5Zn_8. However, the precursors of the 1-cycle and 4-cycle specimens treated at a selenisation temperature of 150°C showed no peaks in Raman spectroscopy, indicating that high-quality Se compounds were yet to form on the specimen surface. When the selenisation temperature was increased to 300°C, the XRD measurement showed that the 1-cycle and 4-cycle specimens both might contain Se compounds and alloy phase. To further understand the presence of Se compounds as observed in XRD, Raman spectroscopy was carried out, and it was observed that the 1-cycle specimen might contain signals for Cu_xSe, CTSe, and CZTSe, whereas the 4-cycle specimen only exhibited the signal for CZTSe. When the selenisation temperature reached 500°C, the signal for CZTSe (but not Cu_xSe and CTSe) could be observed for the 1-cycle specimen in the XRD and Raman measurements, while only the CZTSe signal was observed for the 4-cycle specimen. In addition, the TEM and UV–vis–NIR measurement results for the 1-cycle specimen also revealed the presence of CTSe. A schematic of the thin-film growth was created based on the results above, as shown in Figure 7(b). The precursor metal layers facilitated the diffusion in the 4-cycle specimen, and hence resulted in better diffusion of the elements, which indeed suppressed the formation of the secondary phase and led to a better film quality.

Figure 8(a) shows the dark current (I_{dark}) values of CZTSe solar cells measured at room temperature without illumination, and the J–V curves with AM1.5G (front incident light), where the CZTSe solar cells contained absorber thin films composed of the 1-cycle and 4-cycle specimens. The properties of the devices are listed in Table 2. It can be seen from Table 2 that without illumination, the CZTSe solar cell prepared with the 1-cycle specimen had a shunt resistance (R_{sh}) that was far lower than that of the CZTSe solar cell prepared with the 4-cycle specimen, while the two had similar series resistance (R_s) values. This was mainly because the absorber layer of the CZTSe solar cell composed of the 1-cycle specimen

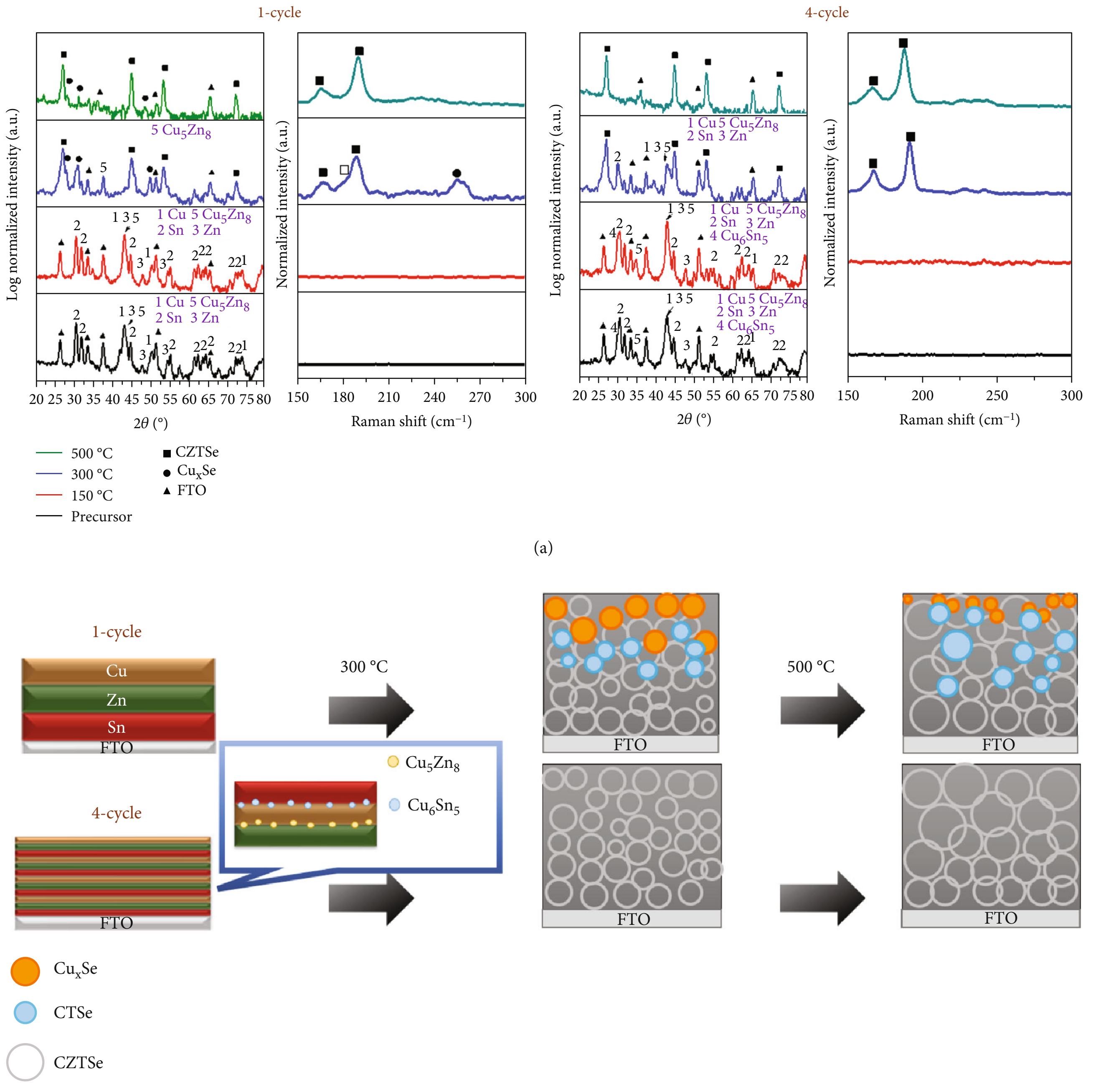

(a)

(b)

Figure 7: (a) XRD and Raman measurements of the 1-cycle-P specimen and 4-cycle-P specimen at different stages of selenisation; (b) schematic diagram of CZTSe thin-film growth mechanism.

contained secondary phases such as Cu_xSe and CTSe, which caused the formation of electricity leakage within the device, thus affecting the properties of the solar cell. The quality of the junction can be reflected by the junction rectifying characteristics, the numerical value of which is calculated by I_{dark} [0.3 V]/I_{dark} [−0.3 V], based on the magnitude of the current measured under forward bias [48]. The values for junction rectifying characteristics of 1-cycle and 4-cycle specimens were calculated to be 3.91 and 29. A larger value for junction rectifying characteristics indicated better diode performance. Based on the junction rectifying characteristics, the CZTSe solar cell prepared with the 4-cycle specimen exhibited the best rectifying performance.

Under AM1.5G (front incident light), the CZTSe solar cell prepared with the 4-cycle specimen exhibited better photovoltaic properties than the CZTSe solar cell prepared with the 1-cycle specimen. It is worth noting that the open circuit voltage (Voc) of the CZTSe solar cells can be

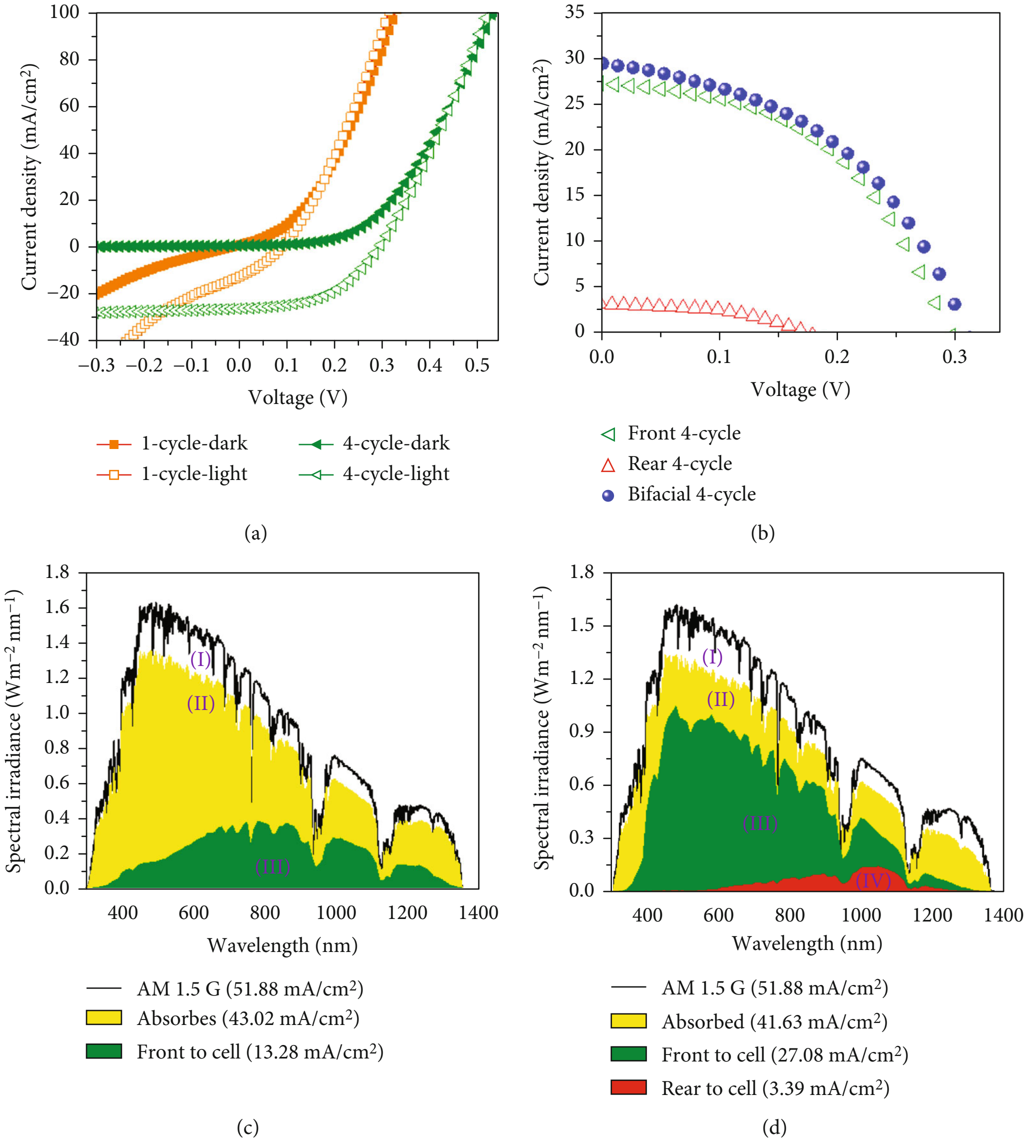

Figure 8: (a) J–V curves without illumination and with AM1.5G (front incident light) for the 1-cycle specimen and 4-cycle specimen, (b) J–V curves of the 4-cycle specimen under different modes of incident light, and (c) spectral irradiance converted from EQE data of charge carriers under front and rear incident light.

Table 2: Photovoltaic properties of solar cells prepared with the 1-cycle and 4-cycle specimens.

		AM1.5G				Dark		
		V_{oc} (V)	J_{sc} (mA/cm^2)	FF (%)	Efficiency (%)	R_{sh} ($\Omega \cdot$cm^2)	R_s ($\Omega \cdot$cm^2)	Junction rectifying character
	Bifacial	N.A.	N.A.	N.A.	N.A.			
1-Cycle	Front	0.09	13.27	33.5	0.4	20	2	3.91
	Rear	N.A.	N.A.	N.A.	N.A.			
	Bifacial	0.31	29.32	45.32	4.13			
4-Cycle	Front	0.3	27.05	47.93	3.89	650	2.2	29
	Rear	0.17	3.3	48.13	0.27			

calculated using the following equation [49]:

$$V_{oc} = \left(\frac{KT}{q}\right) \ln \left(\frac{I_L}{I_0} + 1\right), \quad (3)$$

where K is Boltzmann's constant, T is the temperature, q is the electronic charge, I_L is the light-generated current density, and I_0 is the saturation current density. According to Equation (3), a relatively small saturation current density (I_0) and relatively large light-generated current density (I_L) would result in a relatively high V_{oc}. However, V_{oc} was not affected exclusively by the relationship described in Equation (3). The presence of other secondary phases within the CZTSe absorber layer composed of the 1-cycle specimen not only affected the light-generated current density but also caused an increase in the nonradiative recombination within the absorber layer, thus further reducing V_{oc}. Moreover, the results in Figure 5(d) also show that the energy bandgap of the 4-cycle specimen was larger than that of the 1-cycle specimen, which was consistent with V_{oc}. In terms of the fill factor (FF), the CZTSe solar cell made with the 4-cycle specimen also performed better than that made with the 1-cycle specimen. Generally, a poor FF indicates a relatively large series resistance and small parallel resistance, both of which are caused by the nonuniform distribution of the composition and the impurities in the absorber layer. It can therefore be speculated that the poor FF of the solar cell made with the 1-cycle specimen was a result of the CTSe and Cu_xSe in the absorber layer. Figure 8(b) shows the J–V curves of the CZTSe solar cell prepared with the 4-cycle specimen under front, rear, and bifacial incident light (no measurement could be performed for the solar cell prepared with the 1-cycle specimen under rear incident light). The photovoltaic properties of the solar cells are listed in Table 2. The photovoltaic conversion efficiencies of the CZTSe solar cell prepared with the 4-cycle specimen were 3.89%, 0.27%, and 4.13% under the front, rear, and bifacial incident light, respectively. The improvement in efficiency under bifacial incident light was mainly because the increase in the amount of incident photons triggered a larger light-generated current. It is worth noting that V_{oc} also increased to a certain extent under bifacial incident light, which suggests the absence of significant parasitic junctions in the device (such a junction would have had the opposite polarity of the main junction; for example, the Schottky-like barrier generated on the interface between the FTO back electrode and absorber layer, and the CZTSe/ZnSe junction generated inside the bottom absorber layer). As a result, V_{oc} did not decrease [25, 50].

Figure 8(c) shows the EQE data plots of the spectral irradiance converted to the charge carriers of the CZTSe solar cells prepared with the 1-cycle and 4-cycle specimens. The plots can be divided into four zones for discussion. Zone (I) shows the difference between the AM1.5G spectrum and the spectral irradiance converted from the absorptance rate of the FTO/CZTSe absorber thin film. The AM1.5G spectrum was not fully absorbed in this zone, which was not only due to limitations in the properties of the CZTSe material but also as a result of the transmittance/reflectance of the FTO/CZTSe structure. Zone (II) shows the spectral irradiance converted from the absorber layers of the 1-cycle and 4-cycle specimens. It can be seen that the 1-cycle specimen could convert approximately 82.92% of the AM1.5G spectrum, while the 4-cycle specimen could only convert approximately 80.24%. The difference was mainly due to the presence of CTSe and Cu_xSe inside the absorber film of the 1-cycle specimen. Such secondary phases not only enhanced the absorptance in the visible light region but also maintained a relatively high absorptance in the long wavelength range. Zone (III) shows the spectral irradiance converted from the measured EQE data of the CZTSe solar cells prepared with the 1-cycle and 4-cycle specimens under front incident light. The results showed that the 1-cycle specimen could convert approximately 25.6% of the AM1.5G spectrum, while the 4-cycle specimen could convert approximately 52.2%, which was exactly the opposite of the results in zone (II). This was because although the appearance of CTSe and Cu_xSe inside the absorber layer of the 1-cycle specimen could improve the absorptance, these two materials have relatively high conductivity, which provided leakage paths, while also increasing the possibility of carriers being trapped inside the defects, thereby lowering the light-generated current. Moreover, owing to the ZTO buffer layer, there was a decline due to the lack of CdS absorptance in the range of approximately 375–510 nm. Zone (IV) shows the spectral irradiance converted from the measured EQE data of the CZTSe solar cells prepared with the 4-cycle specimen under rear incident light (no data could be measured for the 1-cycle specimen). Although the rear incident light could be directly absorbed by the absorber layer of the CZTSe solar cell, the electron–hole pairs could not be efficiently separated, making it difficult to generate charge carriers for conduction. When the incident light had a long wavelength, it had a high probability of reaching the space charge region, thus making it possible to generate charge carriers for conduction.

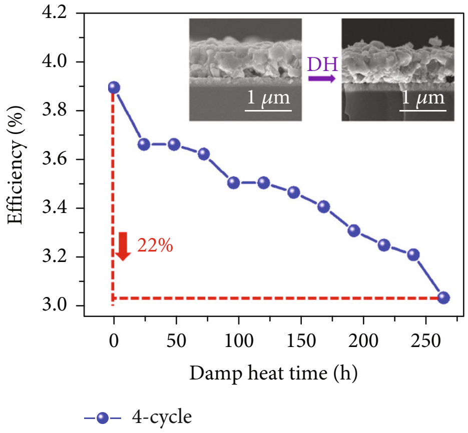

Figure 9: The efficiencies of CZTSe solar cells prepared on FTO substrates obtained during the weatherability DH test. The inset figure is a cross-sectional view of a 4-cycle CZTSe solar cell measured by SEM before and after damp heat treatment.

Figure 9 presents the DH test results of thin-film solar cells with 4-cycle CZTSe specimens under front incident light. DH tests were conducted on the specimens in a standard humidity and heat test environment at 85% RH and 85°C. After 250 h of DH testing, the conversion efficiency decreased from 3.89 to 3.03%, a drop of approximately 22%. This efficiency is approximately 30% [51] lower than the results obtained by Peng et al. using Mo substrate as the back electrode. However, the decrease in efficiency was significant compared with the previous results obtained by our team [14]. Such results were attributed to inadequate optimisation of ZTO buffer layers, which will be addressed in future studies. Moreover, the inset of Figure 9 is the cross-sectional view of the CZTSe solar cell measured by SEM before and after the damp heat treatment. Notably, the thickness, grain size, and structure of the devices were unchanged, which is consistent with previous results reported in the literature [52].

4. Conclusion

In this study, metal precursors were arranged in multistacking metallic layers to improve the thin-film quality of the CZTSe absorber layer. Our findings demonstrated that changing from the original number of stacked layers in 1-cycle-P to that in 4-cycle-P had a significant influence on thin-film quality after selenisation as well as on the characteristics of bifacial photovoltaic devices. The interdiffusion within the stacked metallic layers might promote the formation of (Cu-Sn) alloys, which suppressed the loss of Sn during selenisation, thus further affecting the composition of cations. In addition, secondary phases, including Cu$_x$Se and CTSe, appeared on the top surface and inside the CZTSe thin film of the 1-cycle specimen, leading to poor thin-film quality. In contrast, these secondary phases were not observed in the CZTSe thin film of the 4-cycle specimen, indicating that the metal precursors arranged in a multistacking metallic layer structure could effectively suppress the generation of secondary phases. Finally, this study focused on using an all-vacuum manufacturing technique to improve the continuity of thin-film deposition, as well as to prepare a cadmium-free bifacial CZTSe solar cell. Under bifacial incident light, the bifacial photovoltaic devices obtained had an open-circuit voltage of 0.31 V, a short-circuit current density of 29.32 mA/cm^2, and an efficiency of 4.13%. Therefore, this study has provided not only an important and feasible approach for fabricating CZTSe solar cell structures but also a way to reduce environmental pollution and enhance the continuity of solar modules. Additionally, under DH conditions, the degradation in efficiency was effectively mitigated compared with cells with metal back electrodes reported in other studies.

Data Availability

The authors confirm that the data supporting the findings of this study are available within the article and its supplementary materials.

Conflicts of Interest

The authors declare that they have no conflicts of interest.

Acknowledgments

This research was supported by the Green Technology Research Center of Chang Gung University and also grant funded by Chang Gung Memorial Hospital (BMRP 956), the National Science and Technology Council (NSTC 111-2622-E-182-003), and the Ministry of Science and Technology (MOST 111-2112-M-182-001, MOST 110-2221-E-155-053-MY3).

References

[1] S. Oueslati, G. Brammertz, M. Buffière et al., “Photoluminescence study and observation of unusual optical transitions in Cu$_2$ZnSnSe$_4$/CdS/ZnO solar cells,” *Solar Energy Materials & Solar Cells*, vol. 134, pp. 340–345, 2015.

[2] D.-B. Khadka and J.-H. Kim, “Band gap engineering of alloyed Cu2ZnGexSn1−xQ4 (Q = S, Se) films for solar cell,” *Journal of Physical Chemistry C*, vol. 119, no. 4, pp. 1706–1713, 2005.

[3] M.-S. Kwon, D. Nam, H. Cheong, and C.-W. Jeon, “Effect of cu/(Zn+Sn) ratio on the ZnSe position and performance of CZTSe solar cells,” *Journal of Alloys and Compounds*, vol. 665, pp. 304–310, 2016.

[4] J. Tao, J. Liu, C. Leilei et al., “7.1% efficient co-electroplated Cu2ZnSnS4thin film solar cells with sputtered CdS buffer layers,” *Green Chemistry*, vol. 18, no. 2, pp. 550–557, 2016.

[5] K. Kaur, M. Sood, N. Kumar et al., “Critical role of Zn/Sn ratio to enhance cu-Zn-Sn-S solar cell efficiency by suppressing detrimental Cu$_{2-x}$S secondary phase,” *Solar Energy Materials and Solar Cells*, vol. 179, pp. 22–30, 2018.

[6] K.-J. Yang, D.-H. Son, S.-J. Sung et al., “A band-gap-graded CZTSSe solar cell with 12.3% efficiency,” *Journal of Materials Chemistry A*, vol. 4, no. 26, pp. 10151–10158, 2016.

[7] L. Guo, J. Shi, Q. Yu et al., “Coordination engineering of Cu-Zn-Sn-S aqueous precursor for efficient kesterite solar cells,” *Science Bulletin*, vol. 65, no. 9, pp. 738–746, 2020.

[8] L. Yao, J. Ao, M.-J. Jeng et al., “A CZTSe solar cell with 8.2% power conversion efficiency fabricated using electrodeposited Cu/Sn/Zn precursor and a three-step selenization process at low Se pressure,” *Solar Energy Materials & Solar Cells*, vol. 159, pp. 318–324, 2017.

[9] G. Ren, D. Zhuang, M. Zhao et al., “Cu$_2$ZnSn(S, Se)$_4$ solar cell with slight band tailing states achieves 11.83% efficiency by selenizing sputtered Cu-Zn-Sn-S precursor,” *Journal of Power Sources*, vol. 479, article 228747, 2020.

[10] X. Li, D. Zhuang, Z. Ning et al., “Achieving 11.95% efficient Cu2ZnSnSe4solar cells fabricated by sputtering a Cu–Zn–Sn–Se quaternary compound target with a selenization process,” *Journal of Materials Chemistry A*, vol. 7, no. 16, pp. 9948–9957, 2019.

[11] B. Shin, N.-A. Bojarczuk, and S. Guha, “On the kinetics of MoSe2interfacial layer formation in chalcogen-based thin film solar cells with a molybdenum back contact,” *Applied Physics Letters*, vol. 102, no. 9, article 091907, 2013.

[12] F. Zhou, F. Zeng, X. Liu et al., “Improvement ofJscin a Cu2ZnSnS4solar cell by using a thin carbon intermediate layer at the Cu2ZnSnS4/Mo interface,” *ACS Applied Materials & Interfaces*, vol. 7, no. 41, pp. 22868–22873, 2015.

[13] T. Nakada, Y. Hirabayashi, T. Tokado, D. Ohmori, and T. Mise, “Novel device structure for Cu(In,Ga)Se2 thin film solar cells using transparent conducting oxide back and front contacts,” *Solar Energy*, vol. 77, no. 6, pp. 739–747, 2004.

[14] F.-I. Lai, J.-F. Yang, W.-C. Chen, Y.-C. Hsu, and S.-Y. Kuo, “Weatherability of Cu$_2$ZnSnSe$_4$ thin film solar cells on diverse substrates,” *Solar Energy*, vol. 195, pp. 626–635, 2020.

[15] J. Zhou, X. Xu, B. Duan et al., “Regulating crystal growth via organic lithium salt additive for efficient kesterite solar cells,” *Nano Energy*, vol. 89, article 106405, 2021.

[16] D.-H. Son, S.-H. Kim, S.-Y. Kim et al., "Effect of solid-H2S gas reactions on CZTSSe thin film growth and photovoltaic properties of a 12.62% efficiency device," *Journal of Materials Chemistry A*, vol. 7, no. 44, pp. 25279–25289, 2019.

[17] L.-P. Mwakyusa, L. Lennart, R. Monika et al., "Impact of silver incorporation at the back contact of kesterite solar cells on structural and device properties," *Thin Solid Films*, vol. 709, article 138223, 2020.

[18] Y.-C. Lin and Z.-Y. Su, "Tin-selenium secondary phase etching of Cu2ZnSnSe4: a selective removal route to improve solar cell efficiency," *ACS Applied Energy Materials*, vol. 1, no. 12, pp. 6725–6729, 2018.

[19] K. Mukesh, D. Ashish, A. Nirmal, V. Swaminathan, and Q. Qiquan, "Strategic review of secondary phases, defects and defect-complexes in kesterite CZTS-se solar cells," *Energy & Environmental Science*, vol. 8, pp. 3134–3159, 2015.

[20] W.-S. Liu, S.-Y. Chen, C.-S. Huang, M.-Y. Lee, and H.-C. Kuo, "Investigation of Zn/Sn ratio for improving the material quality of CZTS thin films with the reduction of Cu$_{2-x}$S secondary phase," *Journal of Alloys and Compounds*, vol. 853, article 157237, 2021.

[21] J. Li, Y. Huang, J. Huang et al., "Defect control for 12.5% efficiency Cu2ZnSnSe4 kesterite thin-film solar cells by engineering of local chemical environment," *Advanced Materials*, vol. 32, no. 52, p. 2005268, 2020.

[22] D.-A.-R. Barkhouse, R. Haight, N. Sakai, H. Hiroi, H. Sugimoto, and D.-B. Mitzi, "Cd-free buffer layer materials on Cu2ZnSn(SxSe1−x)4: band alignments with ZnO, ZnS, and In2S3," *Applied Physics Letters*, vol. 100, no. 19, article 193904, 2012.

[23] J. Lee, T. Enkhbat, G. Han et al., "Over 11 % efficient eco-friendly kesterite solar cell: effects of S-enriched surface of Cu$_2$ZnSn(S,Se)$_4$ absorber and band gap controlled (Zn,Sn)O buffer," *Nano Energy*, vol. 78, article 105206, 2020.

[24] A. Ismail, J.-W. Cho, S.-J. Park, Y.-J. Hwang, and B.-K. Min, "Synthesis of solution-processed Cu2ZnSnSe4thin films on transparent conducting oxide glass substrates," *Bulletin of the Korean Chemical Society*, vol. 35, no. 7, pp. 1985–1988, 2014.

[25] J. Ge, J. Chu, J. Jiang, Y. Yan, and P. Yang, "Characteristics of in-substituted CZTS thin film and bifacial solar cell," *ACS Applied Materials & Interfaces*, vol. 6, no. 23, pp. 21118–21130, 2014.

[26] S.-S. Mali, B.-M. Patil, C.-A. Betty et al., "Novel synthesis of kesterite Cu2ZnSnS4 nanoflakes by successive ionic layer adsorption and reaction technique: characterization and application," *Electrochimica Acta*, vol. 66, pp. 216–221, 2012.

[27] E.-R. Moises, S. Diouldé, S. Yudania et al., "Bifacial kesterite solar cells on FTO substrates," *ACS Sustainable Chemistry & Engineering*, vol. 5, pp. 11516–11524, 2017.

[28] J.-S. Kim, J.-K. Kang, and D.-K. Hwang, "High efficiency bifacial Cu2ZnSnSe4thin-film solar cells on transparent conducting oxide glass substrates," *APL Materials*, vol. 4, no. 9, article 096101, 2016.

[29] R.-B.-V. Chalapathy, G.-S. Jung, and B.-T. Ahn, "Fabrication of Cu2ZnSnS4 films by sulfurization of Cu/ZnSn/Cu precursor layers in sulfur atmosphere for solar cells," *Solar Energy Materials & Solar Cells*, vol. 95, no. 12, pp. 3216–3221, 2011.

[30] J.-J. Scragg, T. Ericson, T. Kubart, M. Edoff, and C. Platzer-Björkman, "Chemical insights into the instability of Cu2ZnSnS4films during annealing," *Chemistry of Materials*, vol. 23, no. 20, pp. 4625–4633, 2011.

[31] P.-K. Kannan, C. Sushmita, and R.-D. Suhash, "Detailed investigations on influence of precursor stacking and sulfurization for Cu$_2$ZnSnS$_4$ film formation," *Thin Solid Films*, vol. 649, pp. 81–88, 2018.

[32] W.-C. Chen, C.-Y. Chen, V. Tunuguntla et al., "Enhanced solar cell performance of Cu$_2$ZnSn(S,Se)$_4$ thin films through structural control by using multi-metallic stacked nanolayers and fast ramping process for sulfo-selenization," *Nano Energy*, vol. 30, pp. 762–770, 2016.

[33] E.-A. Brandes and G.-B. Brook, *Smithells Metals Reference Book*, Butterworth-Heinemann, Oxford, 7th ed. edition, 1992.

[34] K.-J. Yang, S. Kim, S.-Y. Kim et al., "Flexible Cu$_2$ZnSn(S,Se)$_4$ solar cells with over 10% efficiency and methods of enlarging the cell area," *Nature Communications*, vol. 10, no. 1, p. 2959, 2019.

[35] Y. Hashimoto, N. Kohara, T. Negami, M. Nishitani, and T. Wada, "Surface characterization of chemically treated cu(in, Ga)Se2thin films," *Japanese Journal of Applied Physics*, vol. 35, no. 9R, pp. 4760–4764, 1996.

[36] C.-J. Wang, S.-C. Shei, and S.-J. Chang, "Synthesis and characterization of CZTSe nanoinks using polyetheramine as solvent," *Optical Materials Express*, vol. 4, no. 8, pp. 1593–1600, 2014.

[37] S. Wang, S. Gao, D. Wang et al., "Room-temperature surface sulfurization for high-performance kesterite CZTSe solar cells," *Solar RRL*, vol. 3, no. 1, p. 1800236, 2019.

[38] J. He, L. Sun, S. Chen, Y. Chen, P. Yang, and J. Chu, "Composition dependence of structure and optical properties of Cu2ZnSn(S,Se)4 solid solutions: an experimental study," *Journal of Alloys and Compounds*, vol. 511, no. 1, pp. 129–132, 2012.

[39] Y. Hirate, H. Tampo, S. Minoura et al., "Dielectric functions of Cu2ZnSnSe4and Cu2SnSe3semiconductors," *Journal of Applied Physics*, vol. 117, no. 1, article 015702, 2015.

[40] B.-K. Yadav, P. Singh, C.-P. Yadav, D.-K. Pandey, and D. Singh, "Structural and wavelength dependent optical study of thermally evaporated Cu2Se thin films," *Zeitschrift für Naturforschung*, vol. 75, no. 9, pp. 781–788, 2020.

[41] S.-G. Choi, J. Kang, J. Li et al., "Optical function spectra and bandgap energy of Cu2SnSe3," *Applied Physics Letters*, vol. 106, no. 4, article 043902, 2015.

[42] Y.-C. Lin, L.-C. Wang, K.-T. Liu, Y.-R. Syu, and H.-R. Hsu, "A comparative investigation of secondary phases and MoSe2 in Cu2ZnSnSe4 solar cells: effect of Zn/Sn ratio," *Journal of Alloys and Compounds*, vol. 743, pp. 249–257, 2018.

[43] N. Serpone, D. Lawless, and R. Khairutdinov, "Size effects on the photophysical properties of colloidal anatase TiO2 particles: size quantization versus direct transitions in this indirect semiconductor?," *The Journal of Physical Chemistry*, vol. 99, no. 45, pp. 16646–16654, 1995.

[44] B.-G. Suresh, Y.-B. Kishore Kumar, B. P. Uday, and R.-V. Sundara, "Effect of Cu/(Zn+Sn) ratio on the properties of co-evaporated Cu$_2$ZnSnSe$_4$ thin films," *Solar Energy Materials and Solar Cells*, vol. 94, no. 2, pp. 221–226, 2010.

[45] B. Ananthoju, J. Mohapatra, M.-K. Jangid, D. Bahadur, N.-V. Medhekar, and M. Aslam, "Cation/anion substitution in Cu2ZnSnS4 for improved photovoltaic performance," *Scientific Reports*, vol. 6, no. 1, 2016.

[46] X. Yin, C. Tang, L. Sun, Z. Shen, and H. Gong, "Study on phase formation mechanism of non- and near-stoichiometric Cu2ZnSn(S,Se)4film prepared by selenization of Cu–Sn–Zn–S precursors," *Chemistry of Materials*, vol. 26, no. 6, pp. 2005–2014, 2014.

[47] J. R. González-Castillo, O. Vigil-Galán, E. Rodríguez, D. Jiménez-Olarte, and J. J. Leal, “Cu6Sn5 binary phase as a precursor material of the CZTSe compound: optimization of the synthesis process, physical properties and its performance as an absorbing material in a solar cell,” *Materials Science in Semiconductor Processing*, vol. 134, article 106016, 2021.

[48] T. Ren, R. Yu, M. Zhong, J.-Y. Shi, and C. Li, “Microstructure evolution of $CuInSe_2$ thin films prepared by single-bath electrodeposition,” *Solar Energy Materials & Solar Cells*, vol. 95, no. 2, pp. 510–520, 2011.

[49] P. Lin, L. Lin, J. Yu, S. Cheng, P. Lu, and Q. Zheng, “Numerical simulation of Cu2ZnSnS4 based solar cells with In2S3 buffer layers by SCAPS-1D,” *Journal of Applied Science and Engineering*, vol. 17, pp. 383–390, 2014.

[50] J. Ge, J. Chu, Y. Yan, J. Jiang, and P. Yang, “Co-electroplated kesterite bifacial thin-film solar cells: a study of sulfurization temperature,” *ACS Applied Materials & Interfaces*, vol. 7, no. 19, pp. 10414–10428, 2015.

[51] C.-V. Peng, P. D. Tara, E. Amin, L. Susan, and R. W. Charles, “Stability of CZTS thin film solar cells upon accelerated thermal cycling and damp heat exposure,” in *Conference: Photovoltaic Specialist Conference (PVSC) 2014; IEEE 40th*, Denver, CO, USA, 2014.

[52] M. Theelen, R. Hendrikx, N. Barreau, H. Steijvers, and A. Böttger, “The effect of damp heat-illumination exposure on CIGS solar cells: a combined XRD and electrical characterization study,” *Solar Energy Materials & Solar Cells*, vol. 157, pp. 943–952, 2016.